Inorganic Chemistry

pubs.acs.org/IC

Article

Advances and Property Investigations of an Organic–Inorganic Ferroelectric: (diisopropylammonium)$_2$[CdBr$_4$]

Magdalena Rok,* Przemysław Starynowicz, Agnieszka Ciżman, Jan K. Zaręba, Anna Piecha-Bisiorek, Grażyna Bator, and Ryszard Jakubas

Cite This: *Inorg. Chem.* 2020, 59, 11986–11994

Read Online

ACCESS | Metrics & More | Article Recommendations | Supporting Information

ABSTRACT: The preparation of materials featuring more than one ferroelectric phase represents a promising strategy for controlling electrical properties arising from spontaneous polarization, since it offers an added advantage of temperature-dependent toggling between two different ferroelectric states. Here, we report on the discovery of a unique ferroelectric–ferroelectric transition in diisopropylammonium tetrabromocadmate (**DPAC**, $(C_6H_{16}N)_2[CdBr_4]$) with a T_c value of 244 K, which is continuous in nature. Both phases crystallize in the same polar orthorhombic space group, *Iab*2. The temperature-resolved second-harmonic-generation (SHG) measurements using 800 nm femtosecond laser pulses attest to the polar structure of **DPAC** on either side of the phase transition (PT). The dc conductivity parameters were estimated in both solid phases. The anionic substructure is in the form of $[CdBr_4]^{2-}$ discrete complexes (0D), while in the voids of the structure, the diisopropylammonium cations are embedded. The ferroelectric properties of phases I and II have been confirmed by the reversible pyroelectric effect as well as by *P*–*E* loop investigations. On the basis of the dielectric responses, the molecular mechanism of the PT at 244 K has been postulated to be of mixed type with an indication of its displacive nature.

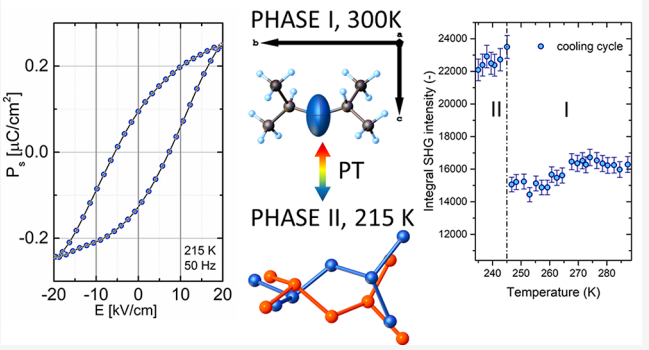

INTRODUCTION

Organic–inorganic hybrid materials have received significant attention not only because of the rich diversity of crystal structures they adopt but also because these systems can be fine-tuned to obtain desirable properties such as light emission,[1−6] semiconductivity,[1,3,7] dielectric switching,[8−11] ferroelectricity,[12,13] and multiferroism.[4−6,14,15] These effects are associated with unique combinations of organic and inorganic components in which usually polar organic cations occupy the voids within the inorganic frameworks. Materials of this type can be therefore understood in terms of host–guest chemistry, in which the host inorganic framework constitutes the defining environment for the rotationally and/or translationally labile guest.

Halometalates stand out as a unique group of stimulus-responsive hybrids, since the organic component is usually more sensitive to the external stimuli, such as temperature and electric or magnetic field strength, resulting in solid to solid structural changes.[16] The behavior, as mentioned above, is typical for both p- and d-block halometalates. Indeed, among the former (and smaller) group one notes a growing body of research on halogenoantimonate(III)[17−20] and halogenobismuthate(III)[17,21−27] networks, while the latter group encompasses a much broader family of halometallates based on divalent or trivalent 3d transition metals. For 3d transition metals, two basic types of stoichiometries can be distinguished: i.e., the tetrahedral building blocks, with a general formula of A_2BX_4, and edge-sharing or face-sharing ABX_3 coordination polymers. Such structures include a large class of hybrids (wherein A = monovalent or divalent organic cation; B = Mn, Fe, Co, Cd, Mn, Cu, Sn, Pb; X = Cl, Br, I),[28−30] with some of them displaying excellent electronic and photoluminescent properties.[31−34]

Technologically relevant properties such as ferroelectricity, semiconductivity, and switching between individual dielectric states are determined primarily by changes in the dynamics of the polar cation near the phase transition (PT) temperature. However, a properly formed anionic subnet favors the creation of the stimuli-responsive organic–inorganic hybrids. As shown in Scheme 1, depending on the synthetic route, one can obtain systems in which halometalates of Cd-X (X = Cl, Br, I) are tetrahedral zero-dimensional (0D) clusters,[2,10,31−34] one-

Received: March 19, 2020
Published: August 15, 2020

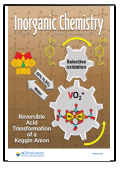

https://dx.doi.org/10.1021/acs.inorgchem.0c00830
Inorg. Chem. 2020, 59, 11986–11994

Scheme 1. Schematic Projection of Inorganic Structures Adopted by Ferroelectric Halocadmates

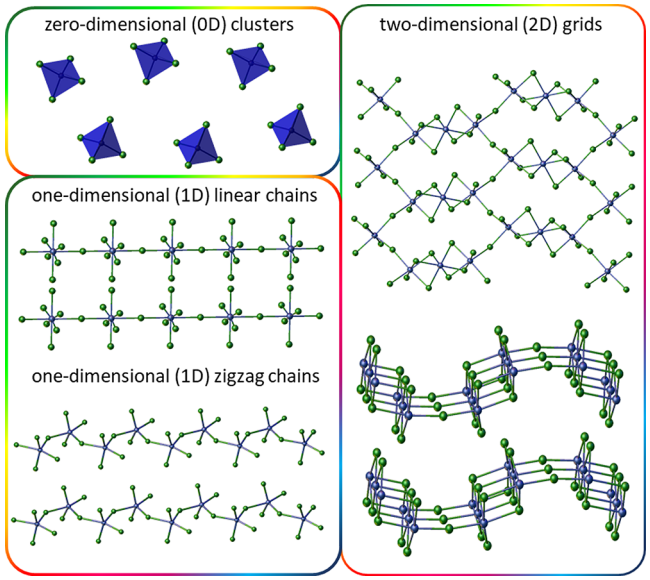

dimensional linear ($1D_L$)[7,16,35−42] or zigzag ($1D_Z$) chains,[43−45] and two-dimensional (2D) grids.[46−51]

Recently, increased interest in the hybrids based on the halo-Cd complexes has been observed due to their photoluminescent properties.[1−3] Specifically, these materials exhibit white-light (WL) emission, rendering them as suitable potential light sources for solid-state-lighting (SSL) applications. Also, some representatives of halogenocadmate(II) hybrids display semiconducting properties, making them applicable in color lighting or displays.[3,7]

If one looks more closely at the currently available library of ferroelectric halocadmates (*vide infra*, Table 1), it is apparent that ferroelectricity was found for each type of structure dimensionality that these compounds can attain. Nevertheless, one structure−property motif is persistent across all of them: namely, $1D_L$ linear halocadmate chains most frequently reveal ferroelectric behavior, while 0D discrete complexes and 2D grids are less often ferroelectric. Quite remarkably, irrespective of the structure dimensionality, all known ferroelectric halocadmates feature a phase transition between noncentrosymmetric and centrosymmetric space groups (i.e., a transition of ferro-paraelectric type), whereas none of them contains more than one ferroelectric phase.

As a part of our studies aimed at the design of room-temperature ferroelectrics, we have synthesized a novel organic−inorganic hybrid, $(C_6H_{16}N)_2[CdBr_4]$ or **DPAC**, whose phase behavior is unique among halocadmates since the structural phase transition (PT) occurs between two polar phases, both of which possess excellent ferroelectric properties. Accordingly, this paper is devoted to the characterization of high (I)- and low-temperature (II) phases of **DPAC** with a particular focus being placed on the exploration of the noncentrosymmetric setting and the ferroelectric property itself. X-ray crystallography and temperature-resolved second-harmonic-generation (TR-SHG) techniques were employed to provide complementary evidence on the acentric structure of both phases. In turn, the ferroelectric nature of phases I and II was evidenced from the pyroelectric investigations and, above all, from the polarization vs electric field (P−E) hysteresis loop measurements. The complex dielectric permittivity measurement led to the determination of a correlation between the microscopic structures and the dielectric relaxation in the investigated phases, while DC measurements allowed us to reveal the semiconducting properties of **DPAC** in the high-temperature range.

EXPERIMENTAL SECTION

Synthesis. Concentrated hydrobromic acid (48% Sigma-Aldrich) was added dropwise to a suspension of $CdCO_3$ (98% Sigma-Aldrich, 3.45 g, 20 mmol) in 10 mL of water. Then diisopropylamine (≥99.5%, Sigma-Aldrich, 4.04 g, 40 mmol) was added dropwise to the solution. By slow evaporation at room temperature, colorless needle crystals of $(C_6H_{16}N)_2[CdBr_4]$ (**DPAC**) were obtained. The composition of the compound was confirmed by elemental analysis. Anal. Found (calcd): C, 22.42 (22.65), N, 4.15 (4.40); H, 4.98 (5.07).

Thermal Analysis. DSC measurements were performed by heating and cooling of the polycrystalline sample in the temperature range of 200−298 K with a ramp rate of 10 K min^{-1} using a Mettler Toledo DSC3 instrument. The TGA/DTA measurements were performed on a Setaram SETSYS 16/18 instrument between 290 and 900 K with a ramp rate of 5 K min^{-1}. The scan was performed under flowing nitrogen (flow rate 1 dm^3 h^{-1}). The melting point was measured with a scanning rate of 10 K min^{-1} using an Opti-Melt MPA-100 instrument in the temperature range from 300 to 480 K. Optical microscopy observations were carried out by using an Olympus BX53 apparatus combined with a LINKAM THM-600 heating/cooling stage, where the temperature was stabilized with an accuracy of 1 K.

Crystal Structure Determination. A suitable crystal was cut from a larger one harvested from the mother liquor. The data collection was performed at room temperature and then for the same crystal at 100 K. The structures were solved routinely with SHELXS and refined with SHELXL-2017. As the space group allows a free origin of the coordinate system along the c axis, the z coordinate of the Cd atom was kept fixed at 0.25 to facilitate an analysis of molecular shifts. All ordered non-H atoms were refined anisotropically and the disordered atoms isotropically, and the positions and U factors of H atoms were constrained. The C−C and C−N distances, as well as the valence angles in the disordered diisopropylammonium cations, were restrained. The data collection and refinement details are presented in Table S1 in the Supporting Information.

Electrical Measurement. All electrical measurements were performed on polycrystalline samples in the form of pressed pellets with various geometrical parameters (S = 20−25 mm^2, d = 0.8−0.4 mm). The complex dielectric permittivity was measured between 200 and 360 K by an Agilent E4980A Precision LCR Meter in the frequency range of 135 Hz to 2 MHz. The electric measurements were carried out under a controlled atmosphere (N_2). The overall errors for the real and imaginary parts of the complex dielectric permittivity were less than 5% and 10%, respectively. The DC conductivity and pyroelectric properties were tested with a Keithley 6517D electrometer/high-resistance meter between 200 and 360 K, with a temperature ramp of 2 K min^{-1}. The ferroelectric hysteresis loops of a polycrystalline powder were obtained by using a modified Sawyer−Tower circuit at a frequency of 50 Hz. The surfaces of the pellet were coated with silver conductive paint (Electron Microscopy Sciences, 503).

Second-Harmonic Generation (SHG). SHG studies were performed using a Quantronix Integra-C regenerative amplifier operating at 800 nm wavelength. This instrument delivers laser pulses of ∼130 fs length and operates at a repetition rate of 1 kHz with an average power of up to 1 W. Prior to measurements, single crystals of **DPAC** and potassium dihydrogen phosphate (KDP, used as a reference for the Kurtz−Perry test) were crushed with a spatula and sieved through a mini-sieve set (Aldrich), collecting a microcrystal size fraction of 88−125 μm. Next, size-graded samples of **DPAC** and KDP were fixed between microscope glass slides

https://dx.doi.org/10.1021/acs.inorgchem.0c00830
Inorg. Chem. 2020, 59, 11986−11994

(forming tightly packed layers) that were sealed and mounted to the holder. The laser beam was directed onto samples at 45° and was unfocused in all cases. Signal-collecting optics, mounted to the glass optical fiber, was placed perpendicularly to the plane of the sample (backscattering geometry). Scattered pumping radiation was suppressed with the use of a 700 nm short-pass dielectric filter (FESH0700, Thorlabs). The attenuation of laser beam intensity was performed with the use of a Glan polarizer. All emission spectra were recorded with an Ocean Optics QE Pro-FL spectrograph. A temperature-resolved SHG (TR-SHG) study (from 287 to 235 K) was conducted using a 800 nm beam with a mean power of 120 mW. In this experiment, the sample was mounted to a custom-made staged Peltier cooling system equipped with an external thermocouple. Spectra were collected for 1000 ms at each temperature point and were averaged five times. The assessment of the SHG efficiency of **DPAC** at 295 K was performed with the use of the Kurtz–Perry technique using KDP as a reference.[52,53] A Kurtz–Perry test was performed using an 800 nm laser beam with a mean power of 320 mW. Spectra were collected for 200 and 2000 ms for KDP and **DPAC**, respectively (averaged five times).

Caution! Work with the high-power laser is dangerous to the eyes, especially in the spectral range in which the beam is invisible. Adequate eye protection should be used during measurements.

RESULTS AND DISCUSSION

Thermal Properties. **DPAC** crystals are stable on exposure to the air up to about 393 K (Figure S1 in the Supporting Information). Beyond this temperature point, a solid to semiliquid PT was observed. This transition also was proven by the melting point measurement (Figure S2a in the Supporting Information) and by the observation of a single crystal under a polarized light microscope (Figure S2b in the Supporting Information). The DSC thermal analysis reveals the presence of one reversible solid to solid PT at 244 K (Figure 1) with a continuous nature. A small value of ΔH_{PT} and a calculated value of ΔS_{PT} equal to ca. 0.5 J/(mol K) suggest a "displacive" mechanism of this structural transformation. Figure S2c in the Supporting Information presents the DSC diagram in the temperature range 150–450 K.

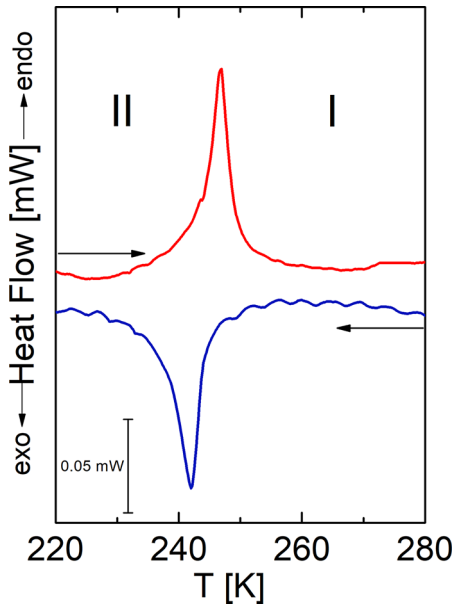

Figure 1. DSC runs obtained upon heating and cooling scans for **DPAC** (sample mass m = 5.812 mg). Black arrows show the directions of runs (cooling or heating at 10 K/min).

Crystal Structures. An analysis of the variable-temperature single-crystal structure reveals an isostructural PT at 244 K. Therefore, the investigations were performed at 100 (phase II) and 293 K (phase I). In both phases, **DPAC** crystallizes in the orthorhombic space group *Iba*2. The basic unit of the crystal is composed of one $CdBr_4$ anion and two disopropylammonium cations (DPA^+) giving an overall A_2BX_4 stoichiometry (see Figure 2a). The Cd ion has a tetrahedral coordination

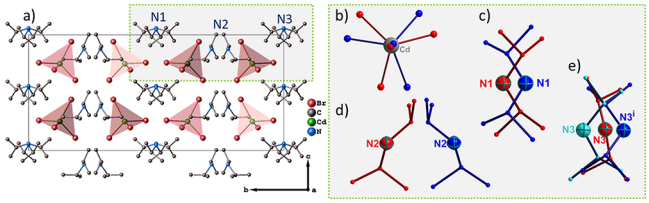

Figure 2. (a) Crystal packing of phase II of **DPAC** viewed along the *a* axis. Movements of the component ions on going from phase I (red atoms and bonds) to phase II (blue or green atoms and bonds; for the sake of clarity only the nitrogen and cadmium atoms have been labeled). (b) Rotation of $[CdBr_4]^{2-}$. The anion from phase I has been shifted so that both Cd atoms overlap. (c) Rotation of the N1 cation along the [100] direction. (d) Transformation of the N2 cation. The (001) plane is perpendicular to the diagram and the N2–N2 direction. (e) Transformation of the N3 cation. The superscript i denotes a $-x$, $-y$, z symmetry operation; the [010] direction runs vertically.

geometry with four adjacent Br atoms. The DPA^+ cations are linked by weak N–H···Br hydrogen bonds with N···Br distances of 3.41–3.64 and 3.38–3.56 Å in phases I and II, respectively (see Table S2 in the Supporting Information). In both phases, the $[CdBr_4]^{2-}$ anions are ordered. As it goes over from phase I to II, the anion rotates approximately around the Cd–Br1 axis; the magnitude of the rotation is about 33° (Figure 2b). The diisopropylammonium cations (types N1 and N2) in phase I are ordered, whereas type N3 is characterized by an enhanced temperature displacement, which may indicate its dynamic disorder. The N1 and N3 atoms are located on 2-fold axes. When the crystal is cooled, the cations undergo the transformations displayed in Figure 2b–e.

In phase II, all organic cations become ordered in terms of a dynamic point of view. Cations of types N1 and N2 change their position in the lattice; the cation N1 as a hole rotates by 180° around the [100] direction (Figure 2c), whereas N2 rotates approximately by 65° around the [120] direction; the rotation angle is defined here as the N–X–C angle at both temperatures (Figure 2d), where XC is the geometric center of the two C atoms bonded to N and, in that, with N3 the nitrogen atom slips off from the 2-fold axis. Cations of type N3 in phase II are now ordered. However, they are statistically distributed between two positions to 50% occupancies (Figure 2e). These positions are related to each other by a rotation of 87° around the [010] direction. This results in the bisector of the H–N–H angle, which probably shows the direction of the most significant contribution to the dipole moment of the diisopropylammonium cation, parallel to the [001] direction at room temperature, becoming approximately oriented along the [100] direction. Additionally, in the N2 and N3 cations, the isopropyl groups rotate around the N–C bonds (approximately by 120°).

Second-Harmonic-Generation (SHG) Effect. The noncentrosymmetric character of phases I and II of **DPAC** is

https://dx.doi.org/10.1021/acs.inorgchem.0c00830
Inorg. Chem. 2020, 59, 11986–11994

strongly suggested by the X-ray diffraction data, but to gain a complete body of evidence on the polarity of both of these phases, we turned to the temperature-resolved second-harmonic-generation (TR-SHG) technique. To do this, we irradiated a size-graded powder of **DPAC** (88−125 μm) with 800 nm femtosecond laser pulses of 120 mW mean power from 287 to 235 K with 2−3 K steps. Figure 3 displays integral

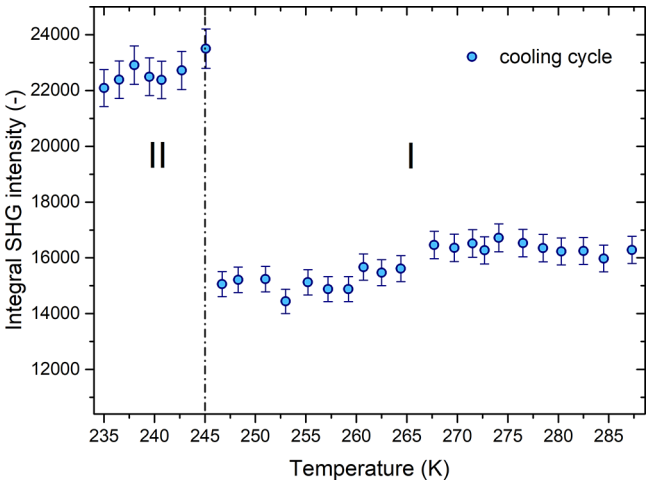

Figure 3. Plot of the integral intensity of the SHG signal of **DPAC** between 235 and 287 K measured on cooling.

intensities of collected SHG signals plotted as a function of temperature; experimental spectra of the SHG response are presented in Figures S3 and S4 in the Supporting Information. It is apparent that upon cooling the SHG signal gradually decreases down to 244 K, at which point it increases in intensity due to the transition to the low-temperature phase I. The downward shift in the integral intensities of the SHG signal, as the cooling progressed, can be attributed to some contribution of laser-induced bleaching of the sample. We have also estimated the relative SHG efficiency for a powdered sample in phase I, with the use of the Kurtz−Perry powder test.[52,53] This test (see spectra of the produced second harmonic of radiation in Figure S5 in the Supporting Information) shows that phase I emits a SHG that is approximately 2 orders of magnitude weaker than that found for KDP of the same particle size (0.013 that of KDP at 295 K). When they are taken as a whole, the collected results confirmed our notion that phases I and II both feature a noncentrosymmetric setting, thus fulfilling the necessary structural prerequisite for ferroelectricity.

Electric Properties. In order to gain information concerning the dynamics of the diisopropylammonium cation, dielectric measurements have been undertaken (Figures 4a,b). In the vicinity of the transition point at 244 K, only a slight change in the slopes of the ε' vs T has been found (see inset in Figure 4a). On the other hand, the significant differences in the dielectric responses regarding relaxation processes between phases I and II should be noted (Figure 4b). In the temperature range between 244 and 300 K, a pronounced, well-shaped dielectric relaxation process is observed, which can be ascribed to the displacement of the diisopropylammonium cation (N3) giving the dipole moment projections on the c as well as the a direction. The frequency dependences of the real part, ε', and the imaginary part, ε'', of dielectric permittivity measured for both phases I and II at several temperatures are presented in Figure S6 in the Supporting Information. Moreover, in phase I (T > 244 K) a significant contribution of the electric conductivity is apparent, while after the transition from phase I to the semiliquid phase this effect is dominant (see Figure S7 in the Supporting Information).

Below the PT temperature, another dielectric anomaly with significantly lower frequency dispersion has been found (see Figure S6 in the Supporting Information). The dielectric response of **DPAC** is well described by using the four-parameter Cole−Cole function[54]

$$\varepsilon^* = \varepsilon' - i\varepsilon'' = \varepsilon_\infty + \frac{\varepsilon_0 - \varepsilon_\infty}{1 + i\omega\tau^{1-\alpha}} \quad (1)$$

where ε_0 and ε_∞ are the low- and high-frequency limits, respectively, ω is the angular frequency, τ is the macroscopic relaxation time, and α represents the relaxation time distribution parameter. Table S3 in the Supporting Information contains the fitting parameters of the Cole−Cole equation at selected temperatures. The macroscopic relaxation times (τ) are presented in Figure 4c, as a logarithmic plot of τ vs reciprocal temperature, $1/T$ (Arrhenius plot). It should be noted that the Arrhenius relationship is well obeyed, which indicates that the reorientations of molecules are thermally

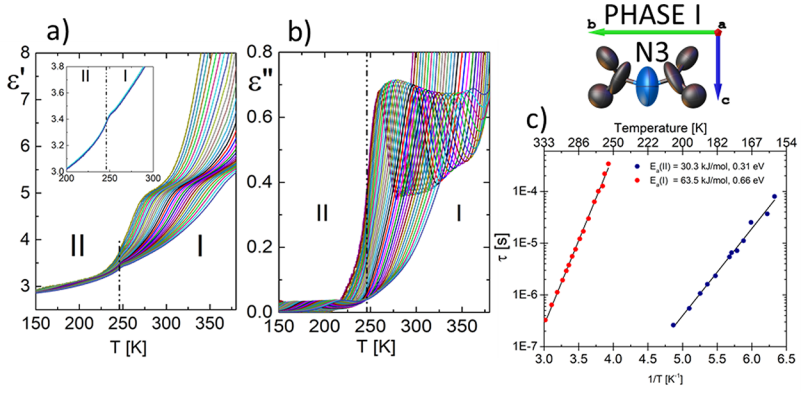

Figure 4. Temperature dependence of the real (a) and imaginary (b) parts of the complex electric permittivity, $\varepsilon^* = \varepsilon' - i\varepsilon''$, at selected frequencies in the vicinity of PT at 244 K for the polycrystalline sample of **DPAC**. A dotted line indicates the PT temperature. Inset: ε' measured at 2 MHz. (c) Arrhenius plot for the macroscopic dielectric relaxation time, ln τ vs $1/T$, for **DPAC** in phase I (red circles) and in phase II (blue circles).

https://dx.doi.org/10.1021/acs.inorgchem.0c00830
Inorg. Chem. 2020, 59, 11986−11994

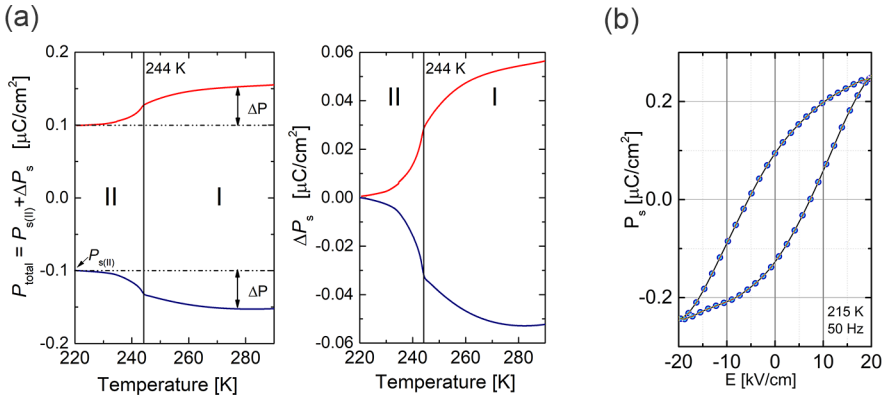

Figure 5. (a) Temperature dependence of P_{total} and ΔP_s after poling by an external electric field (+10 kV/cm, red line; −10 kV/cm, blue line). (b) $P-E$ hysteresis loops obtained at 215 K in phase II.

activated. The estimated activation energy (E_a) value for **DPAC** is equal to 63 (0.66 eV) and 30 (0.31 eV) kJ/mol for phases I and II, respectively. The dielectric response in both phases is strongly diffused—the α values are almost always larger than 0.2. It is surprising that the activation energy E_a for phase I is twice as large as that for phase II. This proves that the dynamics of organic components in phase II is quite different from that in phase I. Since the macroscopic relaxation time (τ) in phase I is longer than that in phase II, and the E_a value is much higher for phase I, some contribution of the long-range interactions between organic cations in phase I may be expected.

The preliminary measurements of the pyroelectric current, I_{pyro}, for a single crystal of **DPAC** show that, first, the pyroelectric current does appear at the PT temperature and, second, it is reversible with temperature (Figure S8a in the Supporting Information) on cooling/heating. The sample was not polarized before the experiment. Due to the rather sensitive nature of the crystals, an application of an external electric field, even at values as low as 50−100 V, resulted in a breakdown of the sample. Nevertheless, the characteristic temperature dependence of I_{pyro} clearly indicates the change of the spontaneous polarization, ΔP_s at 244 K (the PT temperature). Consequently, more detailed studies on ΔP_s have been undertaken. Namely, we decided to apply an external electric field to the polycrystalline sample (pellets) in order to check whether the polarization direction can be reversed. This experiment was performed in such a way that the sample was first polarized in the low-temperature phase II (220 K) and then heated above 244 K. After 1/2 h of shorting the sample, the pyroelectric current was measured on the cooling run. The results of the pyroelectric current measurements are presented in Figure S8b, whereas Figure 5a shows the temperature dependences of ΔP_s calculated from the equation

$$\Delta P_s = \frac{\int I_{pyro}\, dt}{S} \quad (2)$$

where S is a contact area of the sample (in this case of the polycrystalline pellet).

It should be emphasized that, in the pyroelectric experiment, we can measure only a change in the polarization value, ΔP_s; this is why its value at 220 K in Figure 5a is equal to 0. From the hysteresis loop observation, it is obvious that at even lower temperature (215 K) the P_s value is still equal to at least 0.11 $\mu C/cm^2$. In order to determine the origin of the I_{pyro} peak (extrinsic or intrinsic nature), the measurements were repeated at different temperature ramp rates (according to ref 55). Since the sample was in a polycrystalline form, the extrinsic I_{pyro} may be due to the thermally stimulated free charge carriers, and consequently, the broadening of the peak and an increased background, as well as a look only at the I_{pyro} ramp-rate dependence, one may assume an extrinsic origin of the aforementioned effects. As we can see in Figure S9 in the Supporting Information, an integral exclusively of the I_{pyro} peak, observed at 244 K, does not change with the cooling rate, which confirms its intrinsic origin. This means that the value of ΔP_s does not depend on the temperature ramp rate; it is always the same spontaneous polarization value.

In order to confirm the ferroelectric properties of phases I and II of **DPAC**, $P-E$ hysteresis loop measurements were performed. The $P-E$ hysteresis loop at 215 K in phase II is displayed in Figure 5b while that at 298 K (phase I) is given in Figure S10a in the Supporting Information. It is apparent that the polarization can be switched under an ac voltage, 10 kV at 50 Hz ac. **DPAC** also displays a considerable P_s value of 0.11 $\mu C/cm^2$ in phase II (215 K). As was shown in Figure S10b in the Supporting Information, the polarization decreases with a decrease in temperature. As was also pointed out in the SHG and X-ray crystallography sections, **DPAC** is polar in both phases, I and II. It follows that a change in the spontaneous polarization value, ΔP_s, also above T_c close to the PT, should be observed. However, we were not able to record well-shaped rectangular $P-E$ hysteresis loops for phase I of **DPAC** (Figure S10a in the Supporting Information), perhaps due to the significantly higher dielectric losses in comparison to those in phase II and/or a significant contribution of the electric conductivity. It should be emphasized that the hysteresis loop measurements were performed for the polycrystalline samples. Unfortunately, as noted earlier, a further increase in the electric field in order to saturate $P-E$ hysteresis led to a breakdown of the sample; hence, the results presented reflect only the resulting value of ΔP_s and as such should be treated only qualitatively as a confirmation of the polarity of phases II and I of **DPAC**. Nevertheless, the presence and reversibility of ΔP_s, despite its small value, undoubtedly indicate ferroelectricity in both phases of **DPAC**.

We now comment on the effect of the structures of the determined phases on their polar properties. On the basis of the crystal structure data, the unit cells were constructed with the assumption that the positive charge of $[C_6H_{16}N]^+$ and the

https://dx.doi.org/10.1021/acs.inorgchem.0c00830
Inorg. Chem. 2020, 59, 11986−11994

negative charge of $[CdBr_4]^{2-}$ reside on the N atoms and Cd atoms, respectively. According to the point electric charge model (presented in Tables S4 and S5 in the Supporting Information) the center coordinate of negative charge is [0.5,0.5,0.5] in both phases. Meanwhile, the center coordinates of the positive charge are [0.5,0.5,0.43] and [0.5,0.5,0.512], giving the P_s values 2.01 and 0.39 $\mu C/cm^2$ for phases I and II, respectively. In both phases, all dipole moments of the cations, denoted N1−N3, contribute to the resultant spontaneous polarization vector in the crystal lattice. During the transformation, the positions of all cations change significantly with respect to CdB_4^{2-}, which consequently leads to a reduction in the resultant dipole moment and consequently the P_s value. However, a change in the N3 cation dynamics has the greatest effect on the polarity change in the **DPAC** crystal. As we can see in Scheme 2, in phase I the N3 cation is characterized by an increased temperature displacement in either the [100] or [001] direction, as evidenced by the increased C−N−C angle (145.7°) in comparison to the cation N1 (121.1°) or N2 (119.8°). As was motioned above, upon cooling, the N3 cation rotates around the *b* axis by 87° and becomes approximately oriented along the *a* axis. In addition, the cation assumes two positions with 50% occupancies, resulting in an almost antiparallel orientation of the dipole moment. However, the dipole moments of the N3 cation are oriented by an angle of 3° relative to the *a* axis, which means that its projection on the polar *c* axis is much smaller than in the case of phase I. This is also evidenced by the change in the center coordinate of the positive charge of N3 from [0.5,0.5,0.31] calculated for phase I to [0.5,0.5,0.495] in the case of phase II. Therefore, the spontaneous polarization values in phase II have been postulated to decrease.

Scheme 2. Packing Diagram of Organic $(C_6H_{16}N)^+$ Cations Viewed along the *a* Axis with Schematically Marked Dipole Moments

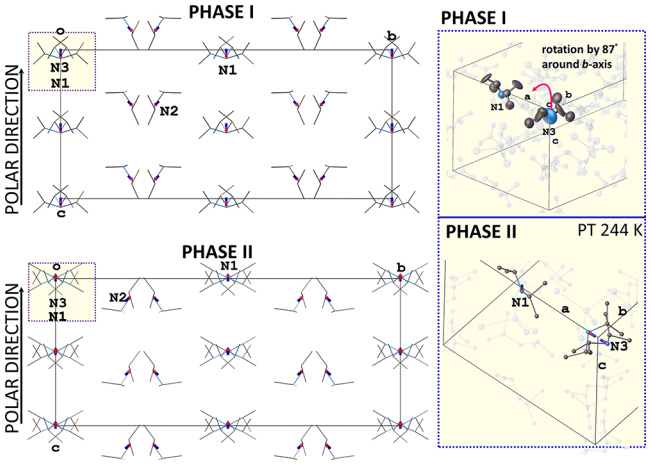

So far, the data collected in Table 1 suggest that, in the case of the hybrids based on Cd-X metallohalides, ferroelectric properties are more often observed in the coordination polymers (predominantly 1D) than in the 0D structures. Also, depending on the type of anion network architecture, for the ABX_3 crystals, larger values of P_s are observed in comparison to those for the A_2BX_4 crystals. During the PT, the **DPAC** crystal still reveals ferroelectric properties. However, the decrease in the P_s value in phase II is related to the mutual displacement in the 244 K PT of the cationic network with respect to the anionic network. The experimental polarization values at 100 and 300 K are significantly smaller than those estimated on the basis of a theoretical approach; the estimated P_s value at 300 K is 2.30 $\mu C/cm^2$, and at 100 K it equals 0.39 $\mu C/cm^2$. The differences between the measured and theoretical values are most likely due to the fact that the sample was examined in the form of a polycrystalline pellet, which always causes a smaller P_s value in comparison to that for a single crystal oriented along the polar axis. A similar relationship was observed in the isostructural crystal $(diisopropylammonium)_2[MnBr_4]$.[56] In the analogue with

Table 1. Compilation of the Most Important Parameters Characterizing Structural and Spontaneous Polarization Properties for Ferroelectric Halocadmates of CdX_3 and CdX_4 (X = Cl, Br, I) Stoichiometries[a]

Formula	T_{PT} (K) cool/heat	PT order	type	symmetry change	P_s ($\mu C/cm^2$)	ref
$(PD)[CdCl_3]$	198/218	first	$1D_L$-$1D_L$-$1D_L$	$C2/c \leftrightarrow Cmc2_1 \leftrightarrow Cmcm$	3.6 (210 K)	36
	240/241	second				
$(PL)[CdCl_3]$	316	second	$1D_L$-$1D_L$	$Cmc2_1 \leftrightarrow Cmcm$	5.1 (253 K)	37
$(PL)[CdBr_3]$	235/238	second	$1D_L$-$1D_L$-$1D_L$	$Cmc2_1 \leftrightarrow C2/m1_1 \leftrightarrow Cmcm$	5.65 (223 K)	38
	244/247	second				
$(CPA)[CdCl_3]$	285/300	first	$1D_L$-$1D_L$	$Cc \leftrightarrow Cmcm$	1.7 (280 K)	39
$(CPA)_2[CdBr_4]$	338/340	second	0D-0D	$Pnam \leftrightarrow Pna2_1$	0.57 (293 K)	31
$(CHA)_2[CdCl_4]$	212/215	second	2D-$1D_Z$-$1D_L$	$Cm \leftrightarrow Cmc2_1 \leftrightarrow I222$	10.79[b] (173 K)	43
	349/367	first			15.95[b] (298 K)	
$(TMA)[CdBr_3]$	162/182	first	$1D_L$-$1D_L$	$P6_1 \leftrightarrow P6_3/m$	0.12 (125 K)	40, 57, 58
$(TMC)[CdCl_3]$	390/400	first	$1D_L$-$1D_L$	$Cc \leftrightarrow P6_3/mmc$	6.2 (397 K)	41
$(TMC)[CdBr_3]$	341/346	second	$1D_L$-$1D_L$	$P6_3mc \leftrightarrow P6_3/mmc$	3.5 (298 K)	42
$(TMP)[CdCl_3]$	346/348	second	$1D_L$-$1D_L$	$P6_3 \leftrightarrow P6_3/m \leftrightarrow P6_3/m$	0.43 (323 K)	59
	387	second				
$(PEA)_2[CdI_4]$	297/301	second	0D-0D	$P2_1 \leftrightarrow P2_1/m$	0.20 (270 K)	60
$(DPA)_2[CdBr_4]$	242/244	second	0D-0D	$Iab2 \leftrightarrow Iab2$	0.11? (2.01[b]) (215 K)	c

[a]Abbreviations: PD, pyrrolidinium; PL, 3-pyrrolinium; CPA, cyclopentylammonium; CHA, cyclohexylammonium; TMA, tetramethylammonium; TMC, trimethylchloromethylammonium; DPA, diisopropylammonium; PEA, 2-phenylethylammonium; TMP, tetramethylphosphonium, first, first-order PT, second, second-order PT; 0D, zero-dimensional clusters; $1D_L$, one-dimensional linear chains; $1D_Z$, one-dimensional zigzag chains; 2D, two-dimensional grids. [b]Theoretical calculation. [c]This work.

https://dx.doi.org/10.1021/acs.inorgchem.0c00830
Inorg. Chem. 2020, 59, 11986−11994

Mn(II), the registered loops were also unsaturated, and the measured values (3.3 $\mu C/cm^2$) were much smaller than the theoretical values calculated on the basis of a simple point electric charge calculation (8.72 $\mu C/cm^2$), despite the fact that the measurements were made on a single crystal.

Figure 6 shows the results of the direct current conductivity, σ_{dc}, for the polycrystalline **DPAC** plotted vs reciprocal temperature, $1/T$. A small change in σ_{dc} is observed at the 244 K PT. However, above 393 K, the conductivity increases significantly. This increase is associated with the transition from the solid to the semiliquid phase of **DPAC**. The estimation of the activation energy, E_a, in the temperature range 250−400 K, according to the Arrhenius relationship

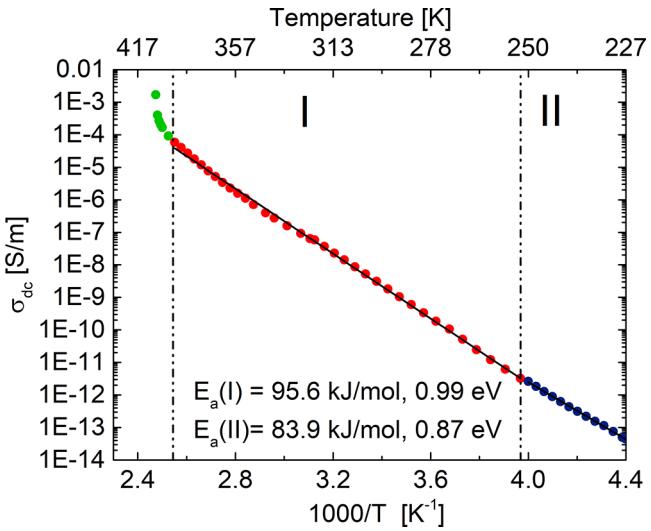

Figure 6. dc conductivity, σ_{dc}, for **DPAC** plotted versus reciprocal temperature, $1000/T$.

$$\sigma_{dc} = \sigma_o \exp\left(\frac{E_a}{RT}\right) \quad (3)$$

where R is a gas constant and σ_o is the conductivity for $T \rightarrow \infty$, shows that E_a differs for phases I and II and equals 97 (0.99 eV) and 84 (0.87 eV) kJ/mol for phases I and II, respectively. In phase I, particularly above room temperature, the **DPAC** crystal shows semiconducting properties and σ_{dc} approaches a value on the order of 10^{-5} S/m.

CONCLUSION

In summary, we have successfully demonstrated a novel rare example of a ferroelectric with an A_2BX_4 stoichiometry, which exhibits an isostructural PT at 244 K. Phases I and II both possess polar properties. The acentricity of these phases was confirmed by SHG measurements, while their polarity was confirmed by the polarization reversal process, in both the pyroelectric effect and hysteresis loop measurements, triggered by an application of an external electric field. In the crystal structure of **DPAC** there are zero-dimensional (0D) clusters with $[CdBr_4]^{2-}$ tetrahedral units. On the basis of both the crystallographic analysis and DSC results, i.e. a slight change in the PT entropy (0.58 J/(mol K)), the structural mechanism of PT is ascribed to be of a mixed type with an indication of a displacive nature. From a structural standpoint, the transition is dominated by the change in dynamics and orientation of diisopropylammonium cations. In the case of the low-temperature phase II the overall arrangement of organic cations generates the spontaneous polarization of 0.11 $\mu C/cm^2$ as determined from $P-E$ hysteresis loop measurements. The determination of ferroelectric properties for both phases of **DPAC** raises hopes that compounds featuring an analogous set of polar properties, but with higher values of spontaneous polarization, may be seen as candidate compounds for application in micro- and nanoelectronics, batteries, and energy storage as well as in photovoltaics. Accordingly, the primary thrust of future work is to explore other representatives of the 0D halocadmate family with A_2BX_4 stoichiometry.

ASSOCIATED CONTENT

Supporting Information

The Supporting Information is available free of charge at https://pubs.acs.org/doi/10.1021/acs.inorgchem.0c00830.

TGA-DTA results, crystallographic data, hydrogen bonding interaction data, SHG spectra, and calculation of spontaneous polarization P_s (PDF)

Accession Codes

CCDC 1991347−1991348 contain the supplementary crystallographic data for this paper. These data can be obtained free of charge via www.ccdc.cam.ac.uk/data_request/cif, or by emailing data_request@ccdc.cam.ac.uk, or by contacting The Cambridge Crystallographic Data Centre, 12 Union Road, Cambridge CB2 1EZ, UK; fax: +44 1223 336033.

AUTHOR INFORMATION

Corresponding Author

Magdalena Rok − *Faculty of Chemistry, University of Wrocław, 50-383 Wrocław, Poland;* orcid.org/0000-0001-6206-8391; Email: magdalena.rok@chem.uni.wroc.pl

Authors

Przemysław Starynowicz − *Faculty of Chemistry, University of Wrocław, 50-383 Wrocław, Poland;* orcid.org/0000-0001-7299-4970

Agnieszka Ciżman − *Department of Experimental Physics, Faculty of Fundamental Problems of Technology, Wrocław University of Science and Technology, 50-370 Wrocław, Poland;* orcid.org/0000-0002-8906-4080

Jan K. Zaręba − *Advanced Materials Engineering and Modelling Group, Faculty of Chemistry, Wrocław University of Science and Technology, 50-370 Wrocław, Poland;* orcid.org/0000-0001-6117-6876

Anna Piecha-Bisiorek − *Faculty of Chemistry, University of Wrocław, 50-383 Wrocław, Poland;* orcid.org/0000-0002-0314-4478

Grażyna Bator − *Faculty of Chemistry, University of Wrocław, 50-383 Wrocław, Poland;* orcid.org/0000-0002-0682-4575

Ryszard Jakubas − *Faculty of Chemistry, University of Wrocław, 50-383 Wrocław, Poland;* orcid.org/0000-0002-2464-8309

Complete contact information is available at: https://pubs.acs.org/10.1021/acs.inorgchem.0c00830

Notes

The authors declare no competing financial interest.

https://dx.doi.org/10.1021/acs.inorgchem.0c00830
Inorg. Chem. 2020, 59, 11986−11994

■ ACKNOWLEDGMENTS

The authors are grateful for financial support from the Plenipotentiary of the Government of the Republic of Poland at the JINR in Dubna under Project No. 75/23/2020. J.K.Z. and A.C. acknowledge financial support from the Wroclaw University of Science and Technology.

■ REFERENCES

(1) Yangui, A.; Pillet, S.; Bendeif, E. E.; Lusson, A.; Triki, S.; Abid, Y.; Boukheddaden, K. Broadband Emission in a New Two-Dimensional Cd-Based Hybrid Perovskite. *ACS Photonics* **2018**, *5* (4), 1599−1611.

(2) Roccanova, R.; Ming, W.; Whiteside, V. R.; McGuire, M. A.; Sellers, I. R.; Du, M. H.; Saparov, B. Synthesis, Crystal and Electronic Structures, and Optical Properties of $(CH_3NH_3)_2CdX_4$ (X = Cl, Br, I). *Inorg. Chem.* **2017**, *56* (22), 13878−13888.

(3) Wang, S.; Li, L.; Sun, Z.; Ji, C.; Liu, S.; Wu, Z.; Zhao, S.; Zeb, A.; Hong, M.; Luo, J. A Semi-Conductive Organic-Inorganic Hybrid Emits Pure White Light with an Ultrahigh Color Rendering Index. *J. Mater. Chem. C* **2017**, *5* (19), 4731−4735.

(4) Wojciechowska, M.; Gagor, A.; Piecha-Bisiorek, A.; Jakubas, R.; Cizman, A.; Zaręba, J. K.; Nyk, M.; Zieliński, P.; Medycki, W.; Bil, A. Ferroelectricity and Ferroelasticity in Organic Inorganic Hybrid $(Pyrrolidinium)_3[Sb_2Cl_9]$. *Chem. Mater.* **2018**, *30*, 4597−4608.

(5) Ye, H. Y.; Zhou, Q.; Niu, X.; Liao, W. Q.; Fu, D. W.; Zhang, Y.; You, Y. M.; Wang, J.; Chen, Z. N.; Xiong, R. G. High-Temperature Ferroelectricity and Photoluminescence in a Hybrid Organic-Inorganic Compound: (3-Pyrrolinium)$MnCl_3$. *J. Am. Chem. Soc.* **2015**, *137* (40), 13148−13154.

(6) Zhang, Y.; Liao, W. Q.; Fu, D. W.; Ye, H. Y.; Chen, Z. N.; Xiong, R. G. Highly Efficient Red-Light Emission in an Organic-Inorganic Hybrid Ferroelectric: (Pyrrolidinium)$MnCl_3$. *J. Am. Chem. Soc.* **2015**, *137* (15), 4928−4931.

(7) Zeb, A.; Sun, Z.; Khan, T.; Asghar, M. A.; Wu, Z.; Li, L.; Ji, C.; Luo, J. $CdCl_3$: An ABX_3 Perovskite-Type Semiconducting Switchable Dielectric Phase Transition Material. *Inorg. Chem. Front.* **2017**, *4*, 1485−1492.

(8) Rok, M.; Bator, G.; Zarychta, B.; Dziuk, B.; Repeć, J.; Medycki, W.; Zamponi, M.; Usevičius, G.; Simenas, M.; Banys, J. Isostructural Phase Transition, Quasielastic Neutron Scattering and Magnetic Resonance Studies of Bistable Dielectric Ion-Pair Crystal $[(CH_3)_2NH_2]_2KCr(CN)_6$. *Dalton Trans.* **2019**, *48*, 4190−4202.

(9) Rok, M.; Moskwa, M.; Działowa, M.; Bieńko, A.; Rajnák, C.; Boča, R.; Bator, G. Multifunctional Materials Based on the Double-Perovskite Organic-Inorganic Hybrid $(CH_3NH_3)_2[KCr(CN)_6]$ Showing Switchable Dielectric, Magnetic, and Semi-conducting Behaviour. *Dalton Trans.* **2019**, *48* (44), 16650−16660.

(10) Xu, C.; Zhang, W. Y.; Chen, C.; Ye, Q.; Fu, D. W. Fast and Slow Integrated Single-Molecule Dual Dielectric Switch Based on a Crystal/Flexible Thin Film. *J. Mater. Chem. C* **2017**, *5*, 6945−6953.

(11) Lv, X. H.; Liao, W. Q.; Li, P. F.; Wang, Z. X.; Mao, C. Y.; Zhang, Y. Dielectric and Photoluminescence Properties of a Layered Perovskite-Type Organic-Inorganic Hybrid Phase Transition Compound: $NH_3(CH_2)_5NH_3MnCl_4$. *J. Mater. Chem. C* **2016**, *4* (9), 1881−1885.

(12) Wei, Z.; Liao, W. Q.; Tang, Y. Y.; Li, P. F.; Shi, P. P.; Cai, H.; Xiong, R. G. Discovery of an Antiperovskite Ferroelectric in $[(CH_3)_3NH]_3(MnBr_3)(MnBr_4)$. *J. Am. Chem. Soc.* **2018**, *140* (26), 8110−8113.

(13) Li, P. F.; Liao, W. Q.; Tang, Y. Y.; Ye, H. Y.; Zhang, Y.; Xiong, R. G. Unprecedented Ferroelectric-Antiferroelectric-Paraelectric Phase Transitions Discovered in an Organic-Inorganic Hybrid Perovskite. *J. Am. Chem. Soc.* **2017**, *139* (25), 8752−8757.

(14) Zhang, Y.; Liao, W. Q.; Fu, D. W.; Ye, H. Y.; Liu, C. M.; Chen, Z. N.; Xiong, R. G. The First Organic-Inorganic Hybrid Luminescent Multiferroic: (Pyrrolidinium)$MnBr_3$. *Adv. Mater.* **2015**, *27* (26), 3942−3946.

(15) Cai, H. L.; Zhang, Y.; Fu, D. W.; Zhang, W.; Liu, T.; Yoshikawa, H.; Awaga, K.; Xiong, R. G. Above-Room-Temperature Magnetodielectric Coupling in a Possible Molecule-Based Multiferroic: Triethylmethylammonium Tetrabromoferrate(III). *J. Am. Chem. Soc.* **2012**, *134* (45), 18487−18490.

(16) Mei, G. Q.; Liao, W. Q. Structural Phase Transitions Coupled with Prominent Dielectric Anomalies and Dielectric Relaxation in a One-Dimensional Organic-Inorganic Hybrid Compound $[C_3H_4NS]$-$[CdCl_3]$. *J. Mater. Chem. C* **2015**, *3* (33), 8535−8541.

(17) Jakubas, R.; Sobczyk, L. Phase Transitions in Alkylammonium Halogenoantimonates and Bismuthates. *Phase Transitions* **1990**, *20*, 163−193.

(18) Jakubas, R.; Sobczyk, L. Ferroelectric Phase Transitions in Alkylammonium Halogenoantimonates (III). *Ferroelectrics* **1988**, *78* (1), 69−78.

(19) Zaleski, J.; Jakubas, R.; Galewski, Z.; Sobczyk, L. Structural Phase Transitions in $[(C_2H_5)_4N]_3Sb_2Br_9$ and $[(C_2H_5)_4N]_3Bi_2Br_9$. *Z. Naturforsch., A: Phys. Sci.* **1989**, *44a*, 1102−1106.

(20) Piecha, A.; Pietraszko, A.; Bator, G.; Jakubas, R. Structural Characterization and Ferroelectric Ordering in $(C_3N_2H_5)_5Sb_2Br_{11}$. *J. Solid State Chem.* **2008**, *181*, 1155−1166.

(21) Scott, J. F. Applications of Modern Ferroelectrics. *Science* **2007**, *315* (5814), 954−959.

(22) Wojtaś, M.; Reece, M. J. Dynamics of Ferroelectric Switching of $[H_3CNH_3]_5[Bi_2Br_{11}]$. *J. Appl. Phys.* **2012**, *111* (2), 024108-1-6.

(23) Piecha, A.; Białońska, A.; Jakubas, R. Structure and Ferroelectric Properties of $[C_3N_2H_5]_5[Bi_2Br_{11}]$. *J. Phys.: Condens. Matter* **2008**, *20*, 325224−325233.

(24) Szklarz, P.; Gągor, A.; Jakubas, R.; Zieliński, P.; Piecha-Bisiorek, A.; Cichos, J.; Karbowiak, M.; Bator, G.; Cizman, A. Lead-Free Hybrid Ferroelectric Material Based on Formamidine: $[NH_2CHNH_2]_3Bi_2I_9$. *J. Mater. Chem. C* **2019**, *7* (10), 3003−3014.

(25) Jóźków, J.; Jakubas, R.; Bator, G.; Pietraszko, A. Ferroelectric Properties of $(C_5H_5NH)_5Bi_2Br_{11}$. *J. Chem. Phys.* **2001**, *114* (16), 7239−7246.

(26) Jakubas, R.; Piecha, A.; Pietraszko, A.; Bator, G. Structure and Ferroelectric Properties of $(C_3N_2H_5)_5Bi_2Cl_{11}$. *Phys. Rev. B - Condens. Matter Mater. Phys.* **2005**, *72* (10), 1−8.

(27) Zhang, H. Y.; Wei, Z.; Li, P. F.; Tang, Y. Y.; Liao, W. Q.; Ye, H. Y.; Cai, H.; Xiong, R. G. The Narrowest Band Gap Ever Observed in Molecular Ferroelectrics: Hexane-1,6-Diammonium Pentaiodobismuth(III). *Angew. Chem., Int. Ed.* **2018**, *57* (2), 526−530.

(28) Shi, C.; Han, X.-B.; Zhang, W. Structural Phase Transition-Associated Dielectric Transition and Ferroelectricity in Coordination Compounds. *Coord. Chem. Rev.* **2019**, *378*, 561−576.

(29) Zhang, W.; Xiong, R. G. Ferroelectric Metal-Organic Frameworks. *Chem. Rev.* **2012**, *112* (2), 1163−1195.

(30) Shi, P. P.; Tang, Y. Y.; Li, P. F.; Liao, W. Q.; Wang, Z. X.; Ye, Q.; Xiong, R. G. Symmetry Breaking in Molecular Ferroelectrics. *Chem. Soc. Rev.* **2016**, *45* (14), 3811−3827.

(31) Huang, C.; Luo, X.; Liao, W.; Tang, Y.; Xiong, R. An Above-Room-Temperature Molecular Ferroelectric: $[Cyclopentylammonium]_2CdBr_4$. *Inorg. Chem.* **2020**, *59*, 829.

(32) Lu, J.; Kochi, J. K. Charge-Modulated Associates of Anionic Donors with Cationic π-Acceptors: Crystal Structures of Ternary Synthons Leading to Molecular Wires. *Cryst. Growth Des.* **2009**, *9*, 291−296.

(33) Dhieb, A. C.; Valkonen, A.; Rzaigui, M.; Smirani, W. Synthesis, Crystal Structure, Physico-Chemical Characterization and Dielectric Properties of a New Hybrid Material, 1-Ethylpiperazine-1,4-Diium Tetrachlorocadmate. *J. Mol. Struct.* **2015**, *1102*, 50−56.

(34) Wang, X. L.; Zhou, L.; Ye, Q.; Geng, F. J.; Ye, H. Y.; Fu, D. W.; Zhang, Y. A Spiro-Type Ammonium Based Switchable Dielectric Material with Two Sequential Reversible Phase Transitions above Room Temperature. *RSC Adv.* **2016**, *6* (78), 74117−74123.

(35) Puget, R.; Jannin, M.; De Brauer, C.; Perret, R. Structures of Trimethyloxosulfonium Salts. V. The Catena-Tri-μ-Chloro- Cadmate

https://dx.doi.org/10.1021/acs.inorgchem.0c00830
Inorg. Chem. 2020, 59, 11986−11994

and the Catena-Tri-μ-Bromo-Cadmate. *Acta Crystallogr., Sect. C: Cryst. Struct. Commun.* **1991**, *47* (9), 1803−1805.
(36) Xu, W. J.; He, C. T.; Ji, C. M.; Chen, S. L.; Huang, R. K.; Lin, R. B.; Xue, W.; Luo, J. H.; Zhang, W. X.; Chen, X. M. Molecular Dynamics of Flexible Polar Cations in a Variable Confined Space: Toward Exceptional Two-Step Nonlinear Optical Switches. *Adv. Mater.* **2016**, *28*, 5886−5890.
(37) Ye, H. Y.; Zhang, Y.; Fu, D. W.; Xiong, R. G. An Above-Room-Temperature Ferroelectric Organo-Metal Halide Perovskite: (3-Pyrrolinium)($CdCl_3$). *Angew. Chem., Int. Ed.* **2014**, *53*, 11242−11247.
(38) Li, P. F.; Liao, W. Q.; Tang, Y. Y.; Ye, H. Y.; Zhang, Y.; Xiong, R. G. Unprecedented Ferroelectric-Antiferroelectric-Paraelectric Phase Transitions Discovered in an Organic-Inorganic Hybrid Perovskite. *J. Am. Chem. Soc.* **2017**, *139*, 8752−8757.
(39) Zhang, Y.; Ye, H. Y.; Zhang, W.; Xiong, R. G. Room-Temperature ABX_3-Typed Molecular Ferroelectric: $[C_5H_9\text{-}NH_3]$-$[CdCl_3]$. *Inorg. Chem. Front.* **2014**, *1*, 118−123.
(40) Gesi, K. Ferroelectricity in $(NCH_3)_4CdBr_3$. *J. Phys. Soc. Jpn.* **1990**, *59*, 432−434.
(41) You, Y. M.; Liao, W. Q.; Zhao, D.; Ye, H. Y.; Zhang, Y.; Zhou, Q.; Niu, X.; Wang, J.; Li, P. F.; Fu, D. W.; et al. An Organic-Inorganic Perovskite Ferroelectric with Large Piezoelectric Response. *Science* **2017**, *357*, 306−309.
(42) Liao, W. Q.; Tang, Y. Y.; Li, P. F.; You, Y. M.; Xiong, R. G. Competitive Halogen Bond in the Molecular Ferroelectric with Large Piezoelectric Response. *J. Am. Chem. Soc.* **2018**, *140*, 3975−3980.
(43) Liao, W. Q.; Ye, H. Y.; Fu, D. W.; Li, P. F.; Chen, L. Z.; Zhang, Y. Temperature-Triggered Reversible Dielectric and Nonlinear Optical Switch Based on the One-Dimensional Organic - Inorganic Hybrid Phase Transition Compound $[C_6H_{11}NH_3]_2CdCl_4$. *Inorg. Chem.* **2014**, *53*, 11146−11151.
(44) Jin, J.; Jin, L.; Su, E.-B. Temperature-Induced Isosymmetric Reversible Structural Phase Transition in Catena-[Pyridinium Tris-(μ2-Bromo)-Cadmium(II)]. *CrystEngComm* **2014**, *16* (39), 9284−9290.
(45) Jian, F. F.; Zhao, P. S.; Wang, Q. X.; Li, Y. One-Dimensional Cd Metal String Complex: Synthesis, Structural and Thermal Properties of $[(HPy)_3(Cd_3Cl_9)]_\infty$. *Inorg. Chim. Acta* **2006**, *359* (5), 1473−1477.
(46) Wang, Z.; Lv, X. H.; Liu, Y. L.; Lu, Y.; Chen, H. P.; Ge, J. Z. Prominent Dielectric Transitions in Layered Organic-Inorganic Hybrids: (Isoamyl-Ammonium)$_2CdX_4$ (X = Cl and Br). *Inorg. Chem. Front.* **2017**, *4* (8), 1330−1336.
(47) Han, S.; Liu, X.; Zhang, J.; Ji, C.; Wu, Z.; Tao, K.; Wang, Y.; Sun, Z.; Luo, J. Dielectric Phase Transition Triggered by the Order-Disorder Transformation of Cyclopropylamine in a Layered Organic-Inorganic Halide Perovskite. *J. Mater. Chem. C* **2018**, *6*, 10327−10331.
(48) Liao, W. Q.; Mei, G. Q.; Ye, H. Y.; Mei, Y. X.; Zhang, Y. Structural Phase Transitions of a Layered Organic-Inorganic Hybrid Compound: Tetra(Cyclopentylammonium) Decachlorotricadmate-(II), $[C_5H_9NH_3]_4Cd_3Cl_{10}$. *Inorg. Chem.* **2014**, *53*, 8913−8918.
(49) Chen, H. P.; Shi, P. P.; Wang, Z. X.; Gao, J. X.; Zhang, W. Y.; Chen, C.; Tang, Y. Y.; Fu, D. W. Tunable Dielectric Transitions in Layered Organic-Inorganic Hybrid Perovskite-Type Compounds: $[NH_3(CH_2)_2Cl]_2CdCl_{4-4x}Br_{4x}]$ (x = 0, 1/4, 1). *Dalton Trans.* **2018**, *47* (20), 7005−7012.
(50) Wang, Z.; Lu, Y.; Chen, H. P.; Ge, J. Z. Controllable Structures Designed with Multiple-Dielectric Responses in Hybrid Perovskite-Type Molecular Crystals. *Inorg. Chem.* **2017**, *56* (12), 7058−7064.
(51) Wang, Y.; Ji, C.; Liu, X.; Han, S.; Zhang, J.; Sun, Z.; Khan, A.; Luo, J. (1,4-Butyldiammonium)$CdBr_4$: A Layered Organic-Inorganic Hybrid Perovskite with a Visible-Blind Ultraviolet Photoelectric Response. *Inorg. Chem. Front.* **2018**, *5* (10), 2450−2455.
(52) Graja, A. Production of the Second Harmonic of Light in Ammonium Pentaborate and Other Powdered Piezoelectric Crystals. *Phys. Status Solidi B* **1968**, *27*, K93−K97.
(53) Kurtz, S. K.; Perry, T. T. A Powder Technique for the Evaluation of Nonlinear Optical Materials. *J. Appl. Phys.* **1968**, *39*, 3798−3813.
(54) Cole, K. S.; Cole, R. H. Dispersion and Absorption in Dielectrics I. Alternating Current Characteristics. *J. Chem. Phys.* **1941**, *9*, 341−351.
(55) Dhanasekhar, C.; Das, A. K.; Das, A.; Venimadhav, A. Ferroelectricity in $CaBaCo_4O_7$ by Light Non Magnetic Zn Doping. *J. Phys.: Condens. Matter* **2020**, *32* (38), 385802.
(56) Jiang, C.; Zhong, N.; Luo, C.; Lin, H.; Zhang, Y.; Peng, H.; Duan, C. G. (Diisopropylammonium)$_2MnBr_4$: A Multifunctional Ferroelectric with Efficient Green-Emission and Excellent Gas Sensing Properties. *Chem. Commun.* **2017**, *53* (44), 5954−5957.
(57) Aguirre-Zamalloa, G.; Madariaga, G.; Couzi, M.; Breczewski, T. X-ray Diffraction Study of the Ferroelectric Phase Transition of $(CH_3)_4NCdBr_3$ (TMCB). *Acta Crystallogr., Sect. B: Struct. Sci.* **1993**, *49* (4), 691−698.
(58) Asahi, T.; Hasebe, K.; Gesi, K. Structure of Tetramethylammonium Tribromocadmate in the Ferroelectric Phase. *Acta Crystallogr., Sect. C: Cryst. Struct. Commun.* **1991**, *47* (6), 1208−1210.
(59) Zhou, L.; Shi, P. P.; Liu, X. M.; Feng, J. C.; Ye, Q.; Yao, Y. F.; Fu, D. W.; Li, P. F.; You, Y. M.; Zhang, Y.; et al. An Above-Room-Temperature Phosphonium-Based Molecular Ferroelectric Perovskite, $[(CH_3)_4P]CdCl_3$, with Sb^{3+}-Doped Luminescence. *NPG Asia Mater.* **2019**, *11* (1), 1−15.
(60) Huang, B.; Sun, L. Y.; Wang, S. S.; Zhang, J. Y.; Ji, C. M.; Luo, J. H.; Zhang, W. X.; Chen, X. M. A Near-Room-Temperature Organic-Inorganic Hybrid Ferroelectric: $[C_6H_5CH_2CH_2NH_3]_2[CdI_4]$. *Chem. Commun.* **2017**, *53* (42), 5764−5766.

https://dx.doi.org/10.1021/acs.inorgchem.0c00830
Inorg. Chem. 2020, 59, 11986−11994